Effects of temperature and pressure on the wave responses of deep carbonate reservoirs

Chuantong Ruan[1,2], Fei Li[3], Jing Ba[1,*], José M. Carcione[1,4] and Chunfang Wu[5]

[1] School of Earth Sciences and Engineering, Hohai University, Nanjing 211100, China

[2] School of Mathematics and Statistics, Zhoukou Normal University, Zhoukou 466001, China

[3] Exploration and Development Research Institute of PetroChina Changqing Oilfield Company, Xi'an 710018, China

[4] National Institute of Oceanography and Applied Geophysics (OGS), Trieste 34010, Italy

[5] School of Economics and Management, Shanghai Technical Institute of Electronics & Information, Shanghai 201411, China

*Corresponding author: Jing Ba. E-mail: jba@hhu.edu.cn

Abstract

Deep carbonate reservoirs are subject to *in-situ* conditions of high temperature and high pressure. We consider six water-saturated dolomite specimens from these reservoirs and perform ultrasonic experiments to obtain the P- and S-wave waveforms and velocities under different pressure and temperature conditions. The P-wave attenuation is estimated using the spectral-ratio method. The results show that with the increase of temperature, the velocities slightly decrease and attenuation increases. At effective pressures <40 MPa, the P-wave velocities increase sharply with pressure and then approximately linearly at higher pressures, while attenuation decreases gradually with pressure. The crack porosity as a function of pressure is obtained from the experimental data. The P-wave velocities decrease with this porosity while attenuation shows an opposite behavior. Then, a multiscale poroelasticity model considering micro-, meso- and macro-scale fluid-flow mechanisms is proposed to analyze the effects of the fluid properties, temperature and crack content on the wave responses. The model results agree well with the experimental data at different pressures, which provides a theoretical basis for the analysis of broadband wave velocity dispersion and attenuation phenomena of carbonate reservoirs and underground porous media in general.

Keywords: dolomite, P-wave velocity and attenuation, multiscale rock-physics, crack, pressure and temperature

1. Introduction

Carbonate reservoirs with rich petroleum resources have been widely explored in recent decades (Cao *et al.* 2018). These reservoirs have a complex mineral composition and inhomogeneous spatial distributions, in particular the storage (pore volume) and permeability (Xu & Payne 2009; Mousavi *et al.* 2013). This strong heterogeneity has hindered the application of classical geophysical methods to detect oil and gas

sweet spots. In particular, the effect of pressure and temperature (PT) is important.

Experimental and theoretical studies showed that the PT conditions have significant effects on the wave velocity and attenuation (Adam *et al.* 2009; Jaya *et al.* 2010; Rabbani *et al.* 2017; Borgomano *et al.* 2019). Timur (1968) used ultrasonic experimental data to analyze the effects of different temperatures on P-wave velocity in saturated rocks. On the basis of experimental measurement, Rabbani *et al.* (2017) found that
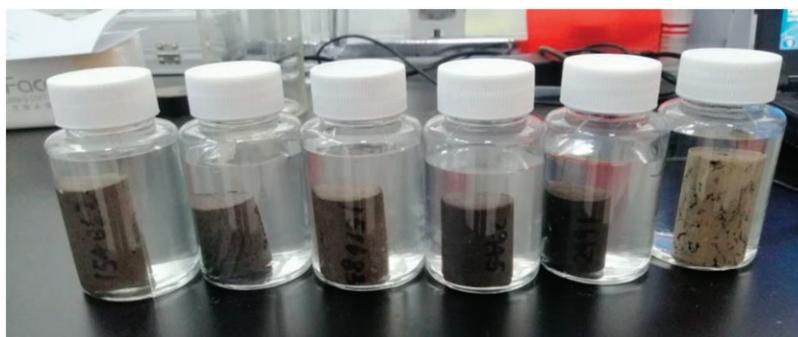
Figure 1. The six dolomite samples.

the attenuation decreased as the temperature decreased from 65 to 15°C. With the increase of temperature, Xi *et al.* (2007) showed that the attenuation peak shifted to high frequency. Jaya *et al.* (2010) carried out experimental measurements on fully saturated basalts in *in-situ* conditions and proposed a velocity-temperature model. Tran *et al.* (2008) observed that the increasing temperature can lead to larger crack density by measuring the Berea sandstone. Chapman *et al.* (2016) measured and analyzed the seismic attenuation of Berea sandstones under different confining pressures, and showed that this property is affected by the pore-fluid flow at mesoscopic scales (the simulation heterogeneity is much longer than the mineral grain size but shorter than the seismic wavelength). All these studies showed that the wave velocity and attenuation depend on the PT conditions and pore-fluid properties.

Owing to the heterogeneities at different scales, it is well known that the main cause for wave dispersion and dissipation are associated with the mechanism of wave-induced fluid flow (WIFF) and elastic scattering (Carcione *et al.* 2003; Müller *et al.* 2010; Guo & Gurevich 2020; Carcione 2022; Guo *et al.* 2022a, 20022b). Many rock-physics models for fully saturated porous media have been proposed to analyze the responses of seismic waves. The first is the Biot global-flow model (Biot 1956a, 1956b), which assumes a macroscopic pore-fluid flow in homogeneous media. However, small-scale heterogeneities have an important effect on wave propagation, in particular attenuation. Mavko & Nur (1975) considered the squirt-flow (microscopic) effect, which is flow between stiff and soft pores. Dvorkin *et al.* (1995) combined squirt-flow theory with Biot theory to put forward the BISQ model, and Gurevich *et al.* (2010) improved this model by means of the equivalent modulus related to frequency (Carcione & Gurevich 2011). Other successful mesoscopic-loss models are the double-porosity ones, for instance, Ba *et al.* (2011) considered the heterogeneity in the mesoscale and proposed the Biot–Rayleigh model.

In the present work, we perform measurements on carbonate samples of the Leikoupo Formation of Sichuan Basin of China and propose a microstructural model to predict the wave responses at different frequencies and PT

**Table 1.** Rock specimen properties

Specimen	Porosity (%)	Permeability (mD)	Density (g/cm^3)
P1	1.41	0.068	2.692
P2	4.26	3.441	2.690
P3	4.44	0.214	2.714
P4	5.93	0.963	2.651
P5	10.37	1.800	2.552
P6	17.35	4.151	2.328

conditions. The theoretical model is a combination of the Biot–Rayleigh (Ba *et al.* 2011) and Gurevich (Gurevich *et al.* 2010) theories. The combined model describes the energy dissipation caused by macroscopic, mesoscopic and microscopic fluid-flow mechanisms. The effects of the PT conditions, fluid properties and crack properties on wave responses are analyzed.

2. Experiments and data processing

The six dolomite samples are cut into cylinders with a diameter of ~25 mm and lengths of 30.1–47.0 mm, as shown in figure 1. Based on the analysis of casting thin sections, the rock has intergranular pores, microcracks and dissolution pores. The porosity varies from 1.41 to 17.35%, and the average is 7.29%. The permeability changes from 0.068 to 4.151 mD, and the average is 1.773 mD. Table 1 shows the physical properties of the six dolomite samples.

The ultrasonic wave transmission technique is adopted to acquire the longitudinal and shear wave velocities (V_P and V_S) of the water-saturated specimens at different temperatures and effective pressures (difference between confining and pore pressures). The vacuum saturation technique is used for saturating the samples, and we put sealed sample into a pressure vessel. Under the condition of pore pressure of 10 MPa and confining pressure of 80 MPa, we perform measurements at room temperature (about 20°C), 40, 60, 80, 100, 115 and 130°C, and record the waveforms. At 130°C and a pore pressure of 10 Mpa, we vary the confining pressures as 80, 70, 60, 50, 40, 30, 25, 20 and 15 MPa.
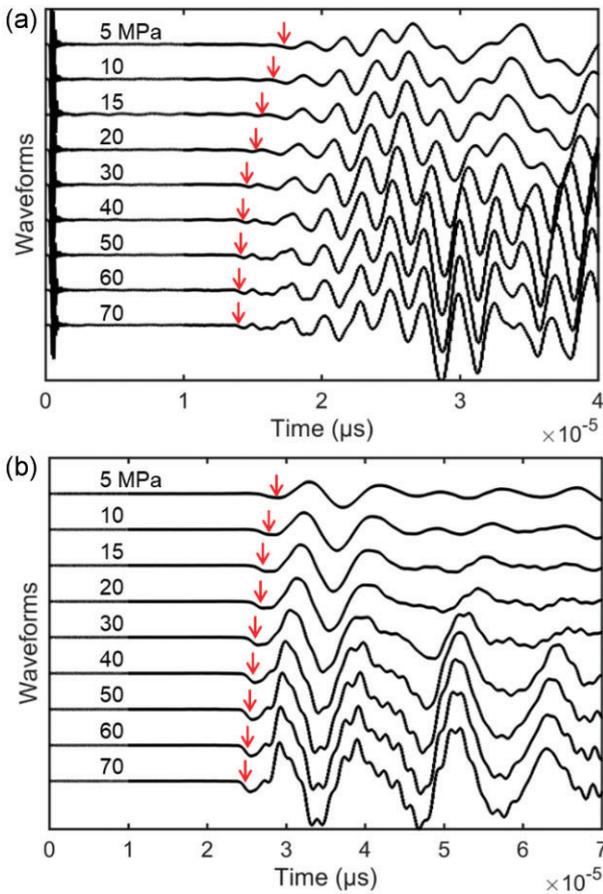
Figure 2. (a) P- and (b) S-wave waveforms corresponding to sample P5 recorded at different effective pressures. The red arrow indicates the position of the first arrival.

Aluminum standards with the same geometrical characteristics of the sample are measured as well. Figure 2 shows the P- and S-waveforms transmitting through sample P5 at different effective pressures. The first arrivals are labeled with red arrows.

V_P and V_S are calculated based on the ratio of sample length to travel time, with an error of <2%. P-wave attenuation $(1/Q_P)$ is obtained by the spectral-ratio method (Toksöz *et al.* 1979). By assuming that the P-wave attenuation is constant nearby the pulse centroid frequency, the quality factor Q_2 of P-wave can be estimated by

$$\ln \frac{A_1}{A_2} = \left(\frac{\pi}{Q_2 v_2} - \frac{\pi}{Q_1 v_1} \right) fx + \ln \frac{G_1}{G_2}, \quad (1)$$

where subscripts 1 2 and correspond to aluminum (reference) and rock sample, respectively, f is the frequency, A denotes the spectrum amplitude, G denotes geometrical factor, v denotes the wave velocity and x is the sample length. The quality factor of aluminum is ~150 000 while the sample quality factor lies generally in the range 10–100. Therefore, $\pi/Q_1 v_1$ is ~0 and the sample quality factor can be obtained
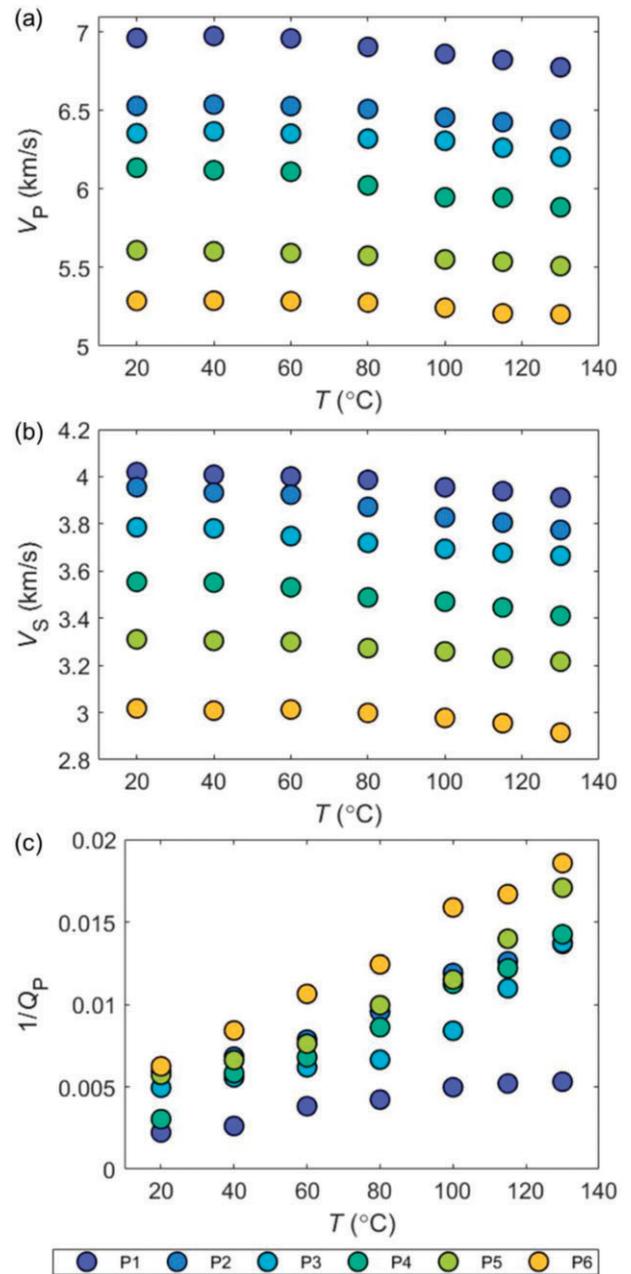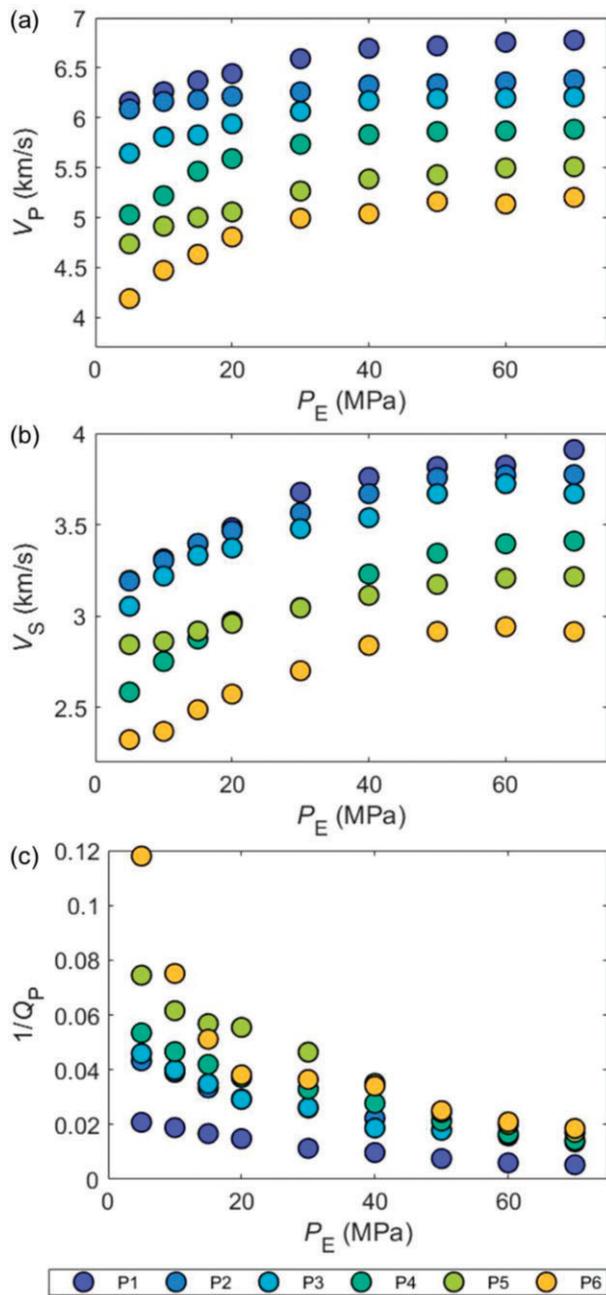

Figure 3. V_P(a), V_S(b) and $1/Q_P$(c) under different temperatures for the six samples.

by the slope coefficient of the linear fitting between the logarithmic spectral ratio and frequency.

3. Wave velocity and attenuation

Under different temperatures for the six samples, figure 3 shows the variation of elastic wave velocities and P-wave attenuation. The average V_P and V_S decrease by 2.51 and 3.47%, respectively, and the attenuation increases by 194% when the temperature increases from 20 to 130°C. Below 60°C, the velocities are approximately constant with temperature and then decrease linearly. The density of water

Figure 4. V_P (a), V_S (b) and $1/Q_P$ (c) under different effective pressures for the six samples.

decreases while its bulk modulus first increases and then decreases with increasing temperature. Attenuation increases and the differences between the sample with the smallest porosity and the other samples also increase with temperature. This may be related to the generation of bubbles and microcracks (Jaya *et al.* 2010).

Figure 4 shows V_P, V_S and $1/Q_P$ under different effective pressures. The average V_P and V_S decrease by 11.45 and 17.72%, respectively, and the attenuation increases by 330% when the effective pressure decreases from 70 to 15 MPa. Below 40 MPa, with the increase of pressure, the wave velocity increases nonlinearly. This is because the soft pores

(microcracks with small aspect ratios) are gradually closed while the stiff pores are not affected, resulting in an increasing bulk modulus (Shapiro 2003). When the effective pressure exceeds 40 MPa, the velocities increase approximately linearly (David & Zimmerman 2012). The increase of effective pressure also hinders the fluid flow between pores and microcracks, causing less energy dissipation. The attenuation varies widely between the different samples at low effective pressures. However, the attenuation values are similar at high effective pressures, indicating that the attenuation is mainly affected by the soft microcracks.

Ideal geometrical shapes, such as ellipsoids, were assumed to characterize complex pore structures (Xu & Payne 2009), where the ratio of the minor and major axes of the ellipsoid is the aspect ratio. The effects of pressure on the number of microcracks and crack shapes are significant, as are shown in figure 5. Soft cracks with smaller aspect ratios are gradually closed first. The crack porosity is estimated with the inversion method proposed by Zhang *et al.* (2019), from the measured velocities (see Appendix A).

The effective pressure dependence of crack porosities is shown in figure 6. The porosities gradually decrease with increasing pressure. Figure 7 shows the changes of V_P and $1/Q_P$ with crack porosity, which decrease and increase with the increase of the porosity, respectively.

4. A multiscale rock-physics model

The complex pore structure hinders the application of classical models for carbonate reservoirs. The WIFF mechanisms at different scales are not independent to each other, and wave attenuation is related to the coupling effects of multiscale fluid flow (Ravalec *et al.* 1996; Tang 2011; Jin *et al.* 2018; Zhang *et al.* 2021, 2022). The Gurevich model considers the effect of squirt flow at the microscopic scale as well as the Biot global (macroscopic) flow (Gurevich *et al.* 2010), while the Biot–Rayleigh (BR) model describes wave dissipation caused at mesoscopic scales and the Biot global flow (Ba *et al.* 2011). Combining these two models we can describe the wave anelasticity at different scales. An illustrative scheme is given in figure 8. It assumes that the host skeleton mainly contains stiff pores while the inclusions contain soft pores (microcracks) and a small number of stiff pores. The Gurevich model is used to obtain the dry-rock modulus of the inclusions.

We make use of the equation of Pride *et al.* (2004) to obtain the bulk modulus and the equation of Lee (2006) to obtain the shear modulus of the host skeleton,

$$K_{b1} = \frac{(1-\phi_{10})K_s}{1+\alpha\phi_{10}}, \tag{2a}$$

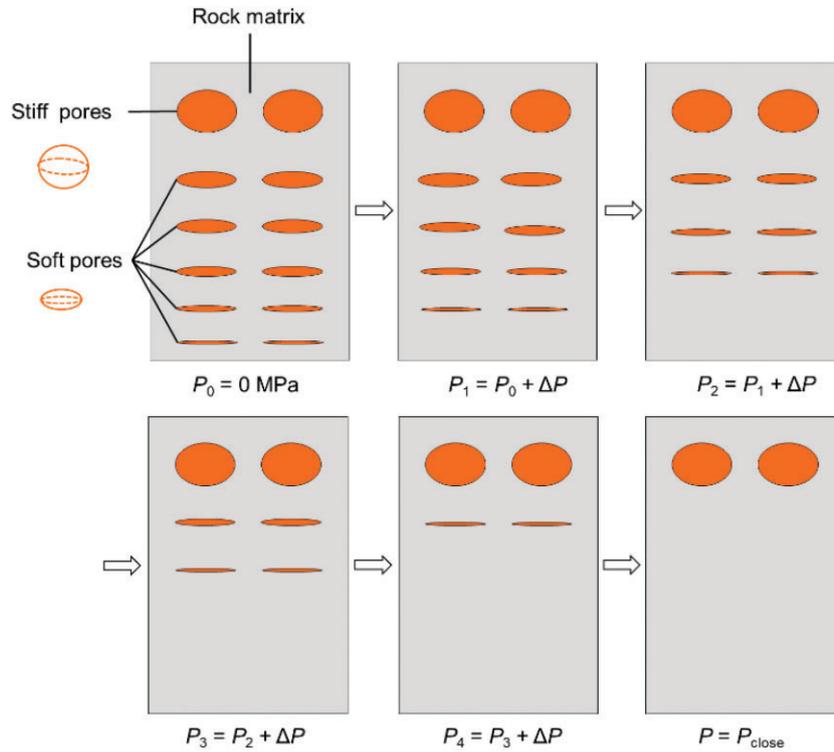$$\mu_{b1} = \frac{(1-\phi_{10})(1+\alpha)\mu_s}{1+\alpha+(1+2\alpha)\alpha\phi_{10}}, \tag{2b}$$

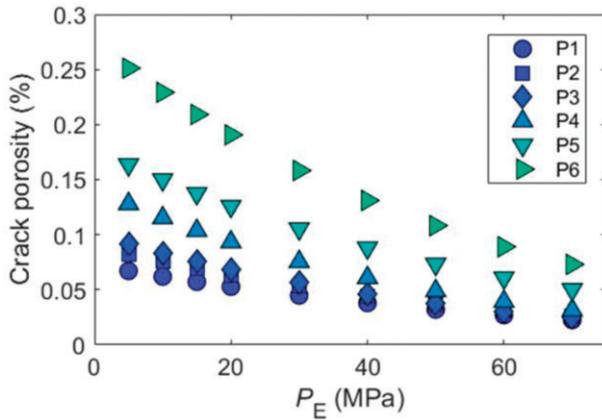**Figure 5.** Diagram showing the behavior of pores and cracks with increasing pressure.

Figure 6. Crack porosity with increasing effective pressure.

Figure 7. The change of V_P (a) and $1/Q_P$ (b) with crack porosity.

respectively, where α is the consolidation coefficient, K_s and μ_s are the bulk and shear moduli of minerals, respectively, and ϕ_{10} is the local porosity of the stiff pores in the host.

We calculate the bulk and shear moduli of the dry skeleton (K_{b2} and μ_{b2}) of the inclusions by means of the Gurevich model,

$$\frac{1}{K_{b2}} = \frac{1}{K_{hp}} + \frac{1}{\frac{1}{\frac{1}{K_{b1}} - \frac{1}{K_{hp}}} + \frac{1}{\left(\frac{1}{K_f^*} - \frac{1}{K_s}\right)\phi_{20}}}, \qquad (3a)$$

$$\frac{1}{\mu_{b2}} = \frac{1}{\mu_{b1}} - \frac{4}{15}\left[\frac{1}{K_{b1}} - \frac{1}{K_{b2}}\right], \qquad (3b)$$
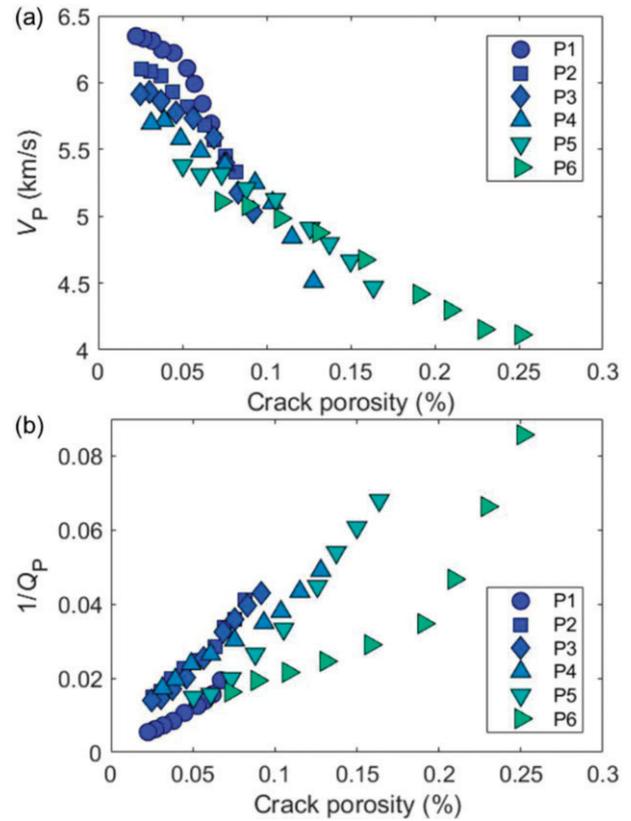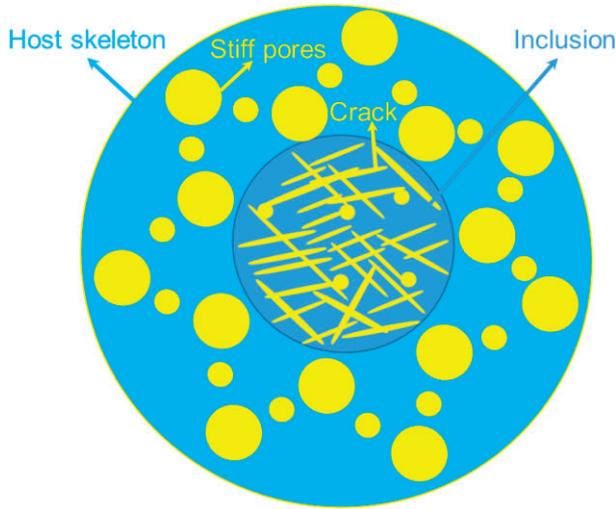
Figure 8. Proposed model with the two types of skeletons and one fluid. The host skeleton contains stiff pores, and the inclusion contains soft pores (cracks) and stiff pores.

where ϕ_{20} is the crack porosity in the inclusions, K_{hp} is the bulk modulus of dry skeleton with all the cracks closed and K_f^*, which is the frequency-related effective bulk modulus of fluid. If there are only stiff pores with no cracks ($\phi_{20} = 0$), equations (3a) and (3b) give $K_{b2} = K_{b1}$ and $\mu_{b2} = \mu_{b1}$, respectively.

The BR model is derived from Hamilton's principle, by considering the dissipation, kinetic and potential energy functions. The crack porosity of host skeleton of the proposed model is zero. Thus, the host skeleton moduli are consistent with these of the conventional BR model. The moduli (K_{b2} and μ_{b2}) replace the bulk and shear moduli of the inclusions in the BR model, leading to the following theoretical equations for wave propagation in the double-porosity model that incorporates the microscopic squirt-flow mechanism.

$$N^G \nabla^2 \mathbf{u} + (A^G + N^G) \nabla \varepsilon + Q_1^G \nabla (\zeta^{(1)} + \phi_2 \varsigma)$$

$$+ Q_2^G \nabla (\zeta^{(2)} - \phi_1 \varsigma) = \rho_{00} \ddot{\mathbf{u}} + \rho_{01} \ddot{\mathbf{U}}^{(1)}$$

$$+ \rho_{02} \ddot{\mathbf{U}}^{(2)} + b_1 (\dot{\mathbf{u}} - \dot{\mathbf{U}}^{(1)}) + b_2 (\dot{\mathbf{u}} - \dot{\mathbf{U}}^{(2)}), \quad (4a)$$

$$Q_1^G \nabla \varepsilon + R_1^G (\zeta^{(1)} + \phi_2 \varsigma) = \rho_{01} \ddot{\mathbf{u}} + \rho_{11} \ddot{\mathbf{U}}^{(1)}$$

$$- b_1 (\dot{\mathbf{u}} - \dot{\mathbf{U}}^{(1)}), \quad (4b)$$

$$Q_2^G \nabla \varepsilon + R_2^G (\zeta^{(2)} - \phi_1 \varsigma) = \rho_{02} \ddot{\mathbf{u}} + \rho_{22} \ddot{\mathbf{U}}^{(2)}$$

$$- b_2 (\dot{\mathbf{u}} - \dot{\mathbf{U}}^{(2)}), \quad (4c)$$

$$\phi_2 (Q_1^G \varepsilon + R_1^G (\zeta^{(1)} + \phi_2 \varsigma)) - \phi_1 (Q_2^G \varepsilon + R_2^G (\zeta^{(2)} - \phi_1 \varsigma))$$

$$= \frac{1}{3} \rho_f \ddot{\varsigma} R_0^2 \frac{\phi_1^2 \phi_2 \phi_{20}}{\phi_{10}} + \frac{1}{3} \frac{\eta \phi_1^2 \phi_2 \phi_{20}}{\kappa_1} \dot{\varsigma} R_0^2. \quad (4d)$$
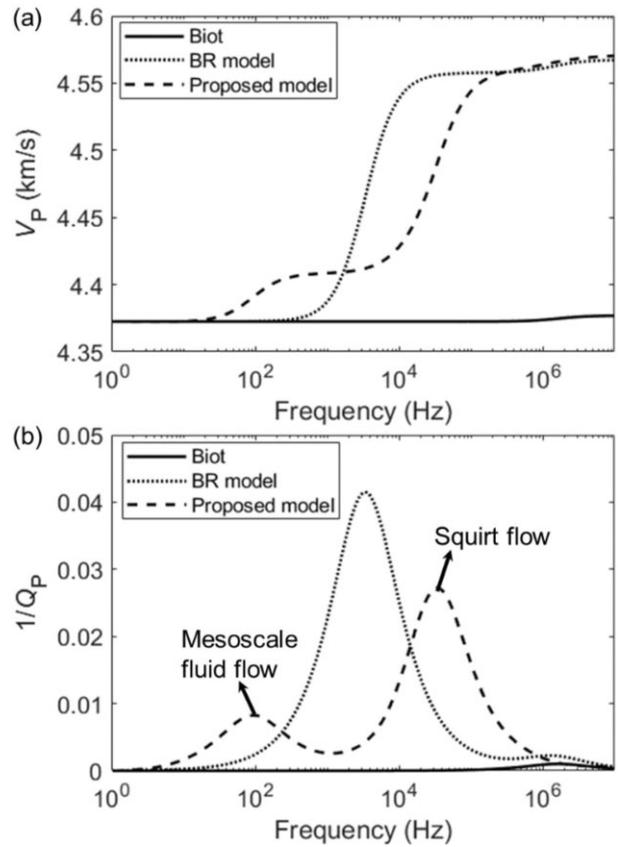
Figure 9. Comparison of V_P (a) and $1/Q_P$ (b) of the three models.

where $\mathbf{u}$ is the particle displacement of the dry-rock skeleton, and $\mathbf{U}^{(1)}$ and $\mathbf{U}^{(2)}$ are the phase 1 and 2 fluid displacements of the host skeleton and inclusions, respectively. $\varepsilon, \zeta^{(1)}$ and $\zeta^{(2)}$ correspond to the three displacement divergence fields; ς is the fluid change due to fluid flow; R_0 is the inclusion radius; ρ_f and η are the fluid density and viscosity; κ_1 is the host permeability; $A^G, N^G, Q_1^G, R_1^G, Q_2^G$ and R_2^G are the elastic stiffnesses; $\rho_{00}, \rho_{01}, \rho_{02}, \rho_{11}$ and ρ_{22} are the density coefficients and b_1 and b_2 represent Biot's dissipation variables. The total porosity is $\phi = \phi_1 + \phi_2$, where $\phi_1 = \nu_1 \phi_{10}$, $\phi_2 = (1 - \nu_1) \phi_{20}$, and ν_1 is the inclusion volume ratio. A plane-wave analysis is given in Appendix B, where the velocity of P-wave and $1/Q_P$ are computed by using the complex wave number derived from the analysis.
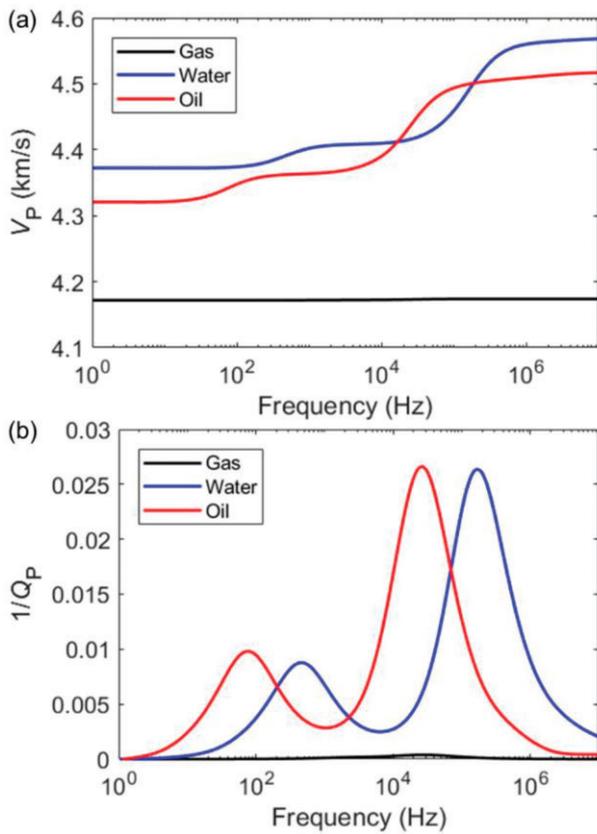
4.1. Comparison of models

We compare the simulation results of the new model with those of the traditional Biot and BR models, and the properties are those of Ba *et al.* (2011), as shown in Table 2. Figure 9 gives the wave velocity and attenuation. At low frequencies, the three models yield the same wave velocities, with the new model predicting two peaks, at seismic and ultrasonic frequencies, as expected, corresponding to attenuation due to mesoscopic and squirt-flow losses, respectively.

Table 2. Physical properties

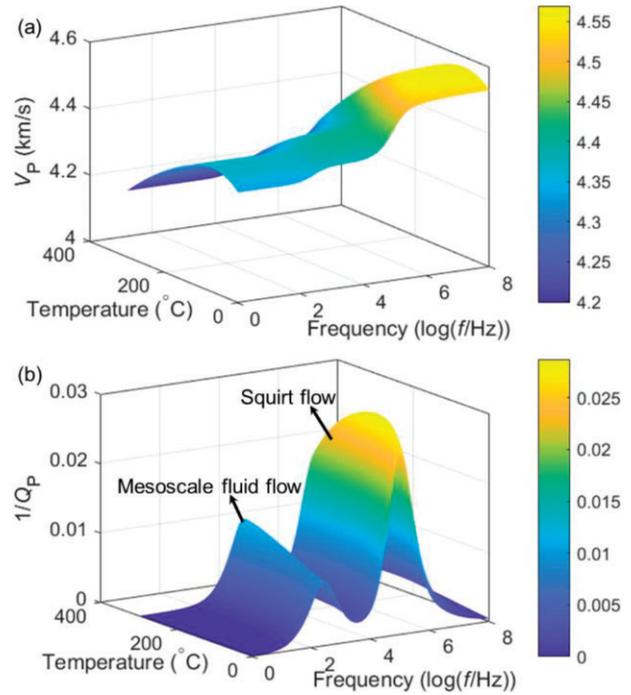| Mineral bulk modulus K_s (GPa)	Mineral shear modulus μ_s (GPa)	Dry-rock density (g/cm³)	Bulk modulus of water K_f (GPa)	Viscosity of water η (Pa·s)	Density of water ρ_f (g/cm³)
38	44	2.65	2.5	0.001	1.04
Porosity of host ϕ_{10}	Porosity of inclusions ϕ_{20}	Permeability of host κ_1 (D)	Permeability of inclusions κ_2 (D)	Volume ratio of inclusions v_1	Radius of inclusions R_0 (m)
0.1	0.3	0.01	1	0.037	0.01

Table 3. Physical properties

	Water	Oil	Gas
Bulk modulus K_f (GPa)	2.25	0.6	0.0001
Density ρ_f (g/cm³)	0.99	0.9	0.1
Viscosity η (Pa·s)	0.001	0.006	0.00 001

Figure 11. V_P (a) and $1/Q_P$ (b) at full water saturation (with a pore pressure of 10 MPa) under different temperatures and frequencies.

Figure 10. V_P (a) and $1/Q_P$ (b) of the model with different fluids at different frequencies.

4.2. Effects of the fluid properties, temperature and pressure

The rock properties are related to various factors such as mineral composition, pore structure, fluid properties and PT conditions. We first consider water, oil and gas as Ba *et al.* (2014) (see Table 3). Figure 10 shows the impact of fluid type on the wave velocity and attenuation. The results show

that the attenuation peaks shift toward lower frequencies as fluid viscosity increases, which is consistent with the models of Wu *et al.* (2020) and Carcione & Gurevich (2011).

The fluid properties vary with PT (see Batzle & Wang 1992). Figure 11 demonstrates the relations between temperature and the frequency-dependence of V_P and $1/Q_P$. The temperature range analyzed is 0–300°C. However, it should be noted that the effect of temperature on rock solid skeleton properties has not been considered. As temperature increases, the V_P shows an initial increase followed by a decrease, with the peak values of attenuation caused by the squirt flow shifting to higher frequencies. The dispersion caused by the mesoscale fluid flow spans a wide frequency band.

The volume fraction of microcracks affects the rock properties. Figure 12 shows the wave responses at different crack porosities. The degree of the peak attenuation at the low-frequency range, caused by the mesoscale fluid flow, increases
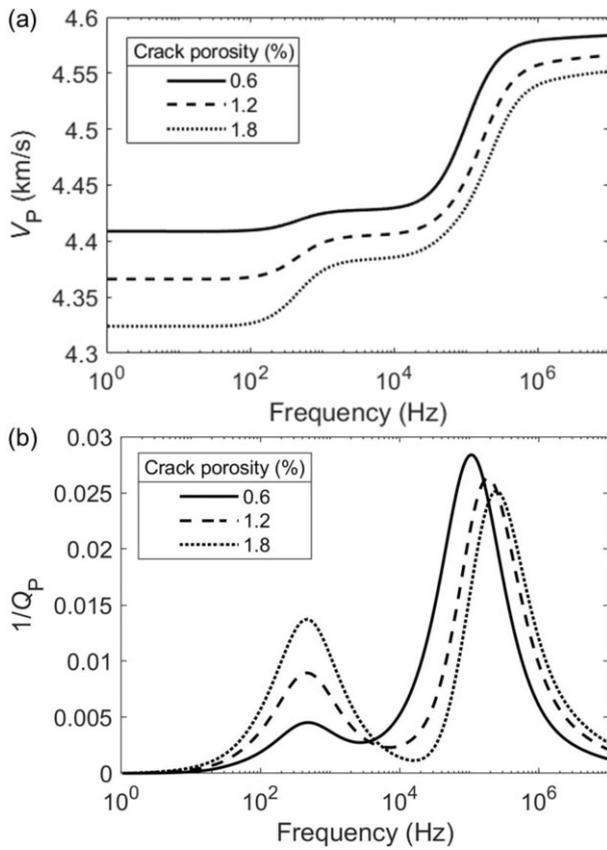
Figure 12. V_P (a) and $1/Q_P$ (b) under different frequencies and crack porosities.
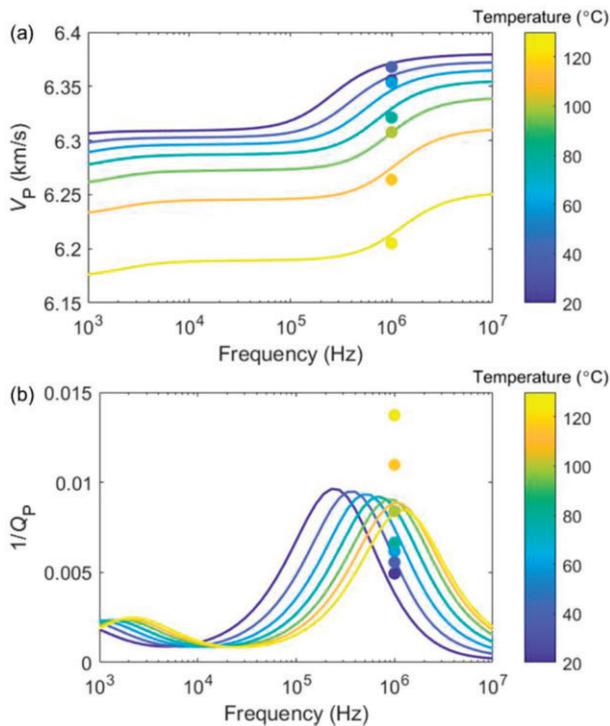
Figure 13. V_P (a) and $1/Q_P$ (b) under different frequencies and temperatures. The dots with the colorbar indicate the measured data.
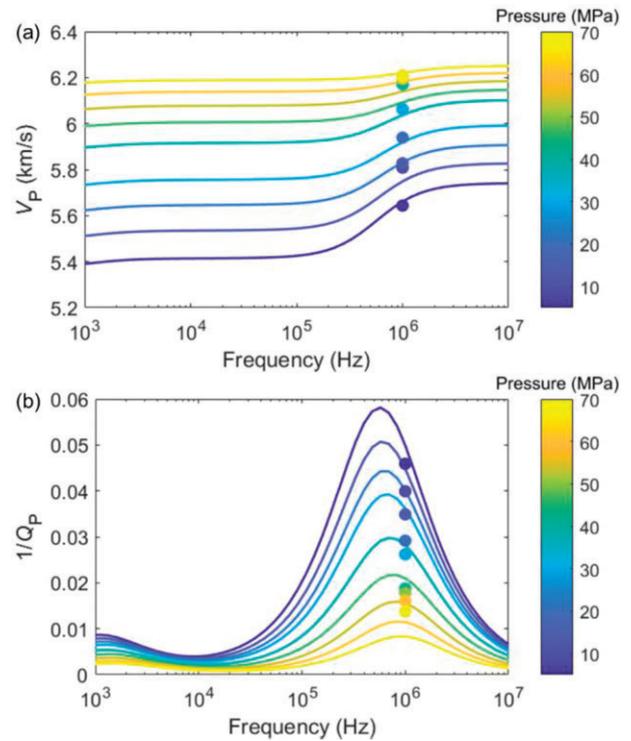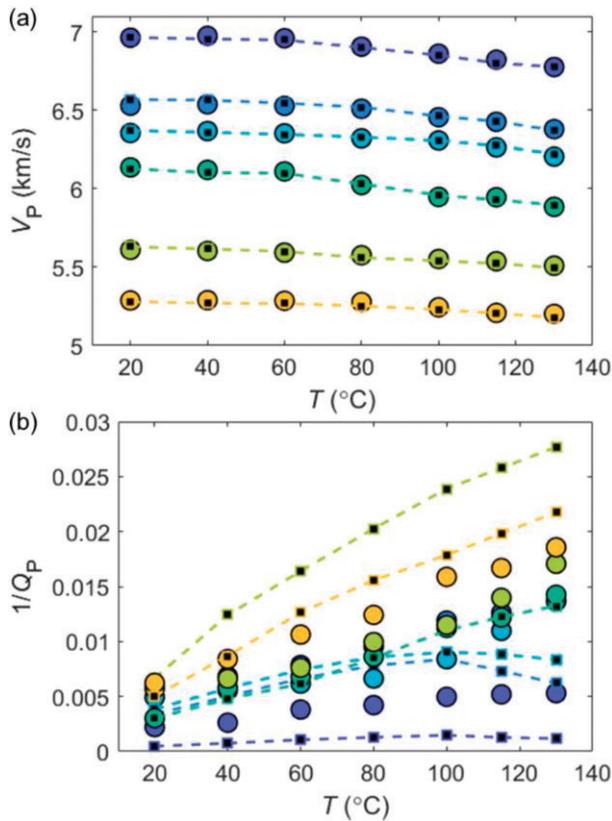

Figure 14. V_P (a) and $1/Q_P$ (b) under different frequencies and effective pressures. The dots with the colorbar indicate the measured data.

with increasing crack porosity, while the peak as a result of the squirt-flow shifts to higher frequencies.

4.3. Comparisons between model predictions and measurements

The proposed Batzle & Wang (1992) equation is used to determine the fluid properties that vary with temperature. The density ρ_f, bulk modulus K_f and viscosity η of water are 0.942 g/cm^3, 2.19 GPa and 0.002 Pa·s at 130°C and a pore pressure 10 MPa, respectively. The crack porosities at different pressures are obtained with figure 6. For sample P3, the mineral bulk modulus K_s is 67 GPa, shear modulus μ_s is 55 GPa and its density is 2.714 g/cm^3. The equations of Lee (2006) and Pride *et al.* (2004) are used to calculate the dry-rock moduli. This sample has a total porosity ϕ of 4.44%, a permeability κ of 0.214 mD, a crack aspect ratio γ of 0.00005 and an inclusion radius R_0 of 0.1 mm.

The density and viscosity of water decrease while its bulk modulus first increases and then decreases as the temperature changes from 20 to 130°C. Figure 13 compares the predicted V_P and $1/Q_P$ values to the experimental data for various frequencies and temperatures. The calculated wave velocities and attenuation are slightly higher and smaller than the measured ones, respectively, particularly at high temperatures. This difference may be due to the generation of thermal cracks, resulting in a smaller bulk modulus and a

Figure 15. V_P (a) and $1/Q_P$ (b) under different temperatures for the six samples. The dots with the colorbar indicate the measured data.

Figure 16. V_P (a) and $1/Q_P$ (b) under different effective pressures for the six samples. The dots with the colorbar indicate the measured data.
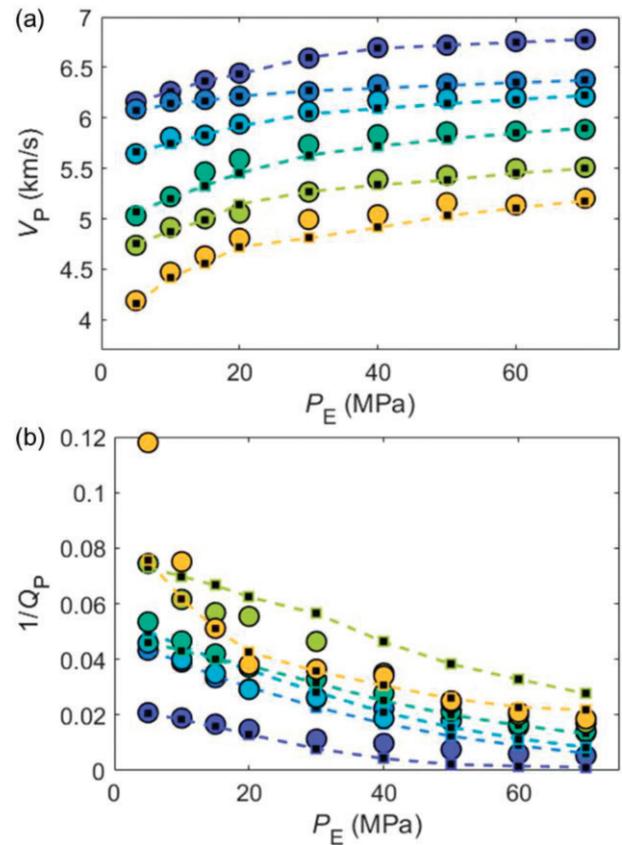
stronger fluid-flow effect. Moreover, the presence of bubbles at high temperatures may also contribute (Jaya *et al.* 2010; Grab *et al.* 2017).

The crack porosities decrease from 0.0919 to 0.0249% in sample P3 when the effective pressure changes from 5 to 70 MPa, as are shown in figure 6. Figure 14 compares theory and experiment at different effective pressures, indicating that the agreement is good for both properties, the wave velocity and attenuation.

Finally, figures 15 and 16 compare the theoretical and experimental V_P and $1/Q_P$ of the six rock samples under different temperatures and effective pressures, respectively. It is shown that the proposed model describes well the P-wave velocity variations, but cannot well explain the temperature dependence of attenuation, possibly due to the effects mentioned before, such as generation of bubbles and thermal cracking at higher temperatures, effects that have not been included in the model.

5. Conclusions

Ultrasonic measurements have been performed on six water-saturated samples collected from the deep carbonate reservoirs, under different temperatures and effective pressures.

With the increase of temperature or the decrease of effective pressure, the P-wave velocities decrease and attenuation increases. Moreover, the P-wave velocities decrease with the increasing crack porosity, while attenuation shows an opposite trend. Then, we propose a multiscale wave-induced fluid-flow model to describe the wave responses of carbonate rocks containing stiff and soft (cracks) pores. The model results show a good agreement with the data but underestimate the attenuation at higher temperatures, which may be associated with the occurrence of thermal cracking and presence of bubbles. Further research is needed to describe these effects. In principle, the proposed model can be used to quantitatively describe the wave velocity and attenuation of deep carbonate reservoirs.

Acknowledgements

Appendix A. Calculation of the crack porosity

Based on the MT model (Mori & Tanaka 1973), the relation between the elastic moduli and stiff pore properties can be obtained. By assuming that the stiff pores are part of the solid matrix, the bulk modulus and shear modulus (with cracks fully closed) are

$$K_{hp} = K_s \bigg/ \left(1 + \frac{\phi_s}{1-\phi_s}P\right), \qquad (A1)$$

$$\mu_{hp} = \mu_s \bigg/ \left(1 + \frac{\phi_s}{1-\phi_s}Q\right), \qquad (A2)$$

where the stiff porosity is ϕ_s, the shape factors associated with the crack aspect ratio γ and Poisson's ratio of grain are represented by P and Q (David & Zimmerman 2012).

The following equations can be used to determine the effective elastic moduli of the dry rock containing stiff pores and cracks.

$$K_{eff} = K_{hp} \bigg/ \left(1 + \frac{16\left(1-\left(v_{hp}\right)^2\right)\Gamma}{9\left(1-2v_{hp}\right)}\right), \qquad (A3)$$

$$\mu_{eff} = \mu_{hp} \bigg/ \left(1 + \frac{32\left(1-v_{hp}\right)\left(5-v_{hp}\right)\Gamma}{45\left(2-v_{hp}\right)}\right), \qquad (A4)$$

where $v_{hp} = (3K_{hp}-2\mu_{hp})/(6K_{hp}+2\mu_{hp})$ is the rock Poisson ratio (with only stiff pores) and the cumulative crack density is denoted by Γ. The wave velocities measured at different pressures are used to compute the moduli. The cumulative crack density is estimated by using a liner fitting method based on equations (A3) and (A4). The crack density Γ_p associated with the effective pressure p_e is (Shapiro 2003)

$$\Gamma_p = \Gamma^i e^{-p_e/\hat{p}_e}, \qquad (A5)$$

where the initial crack density at the effective pressure of zero is Γ^i and a compaction coefficient is $\hat{p}_e$. The crack aspect ratio γ_p associated with the effective pressure is (Zhang *et al.* 2019)

$$\gamma_p = \frac{4(1-v_{hp}^2)p_e}{\pi E_{hp}}, \qquad (A6)$$

where E_{hp} is the effective static Young modulus at the high pressure range. The crack porosity is given by (David & Zimmerman 2012)

$$\phi_2 = \frac{4\pi\gamma_p}{3}\Gamma_p. \qquad (A7)$$

Appendix B. Plane-wave analysis

By substituting plane-wave kernel $e^{i(\omega t - \mathbf{k}\cdot\mathbf{x})}$ into equations (4a)–(4d) with ω, $\mathbf{k}$ and $\mathbf{x}$ as the angular frequency, wave number vector and spatial vector, respectively, a P-wave equation is obtained.

$$\begin{vmatrix} a_{11}k^2 + b_{11} & a_{12}k^2 + b_{12} & a_{13}k^2 + b_{13} \\ a_{21}k^2 + b_{21} & a_{22}k^2 + b_{22} & a_{23}k^2 + b_{23} \\ a_{31}k^2 + b_{31} & a_{32}k^2 + b_{32} & a_{33}k^2 + b_{33} \end{vmatrix} = 0, \qquad (B1)$$

where

$$\begin{aligned}
a_{11} &= A^G + 2N^G + i\left(Q_2^G\phi_1 - Q_1^G\phi_2\right)x_1, \\
a_{12} &= Q_1^G + i\left(Q_2^G\phi_1 - Q_1^G\phi_2\right)x_2, \\
a_{13} &= Q_2^G + i\left(Q_2^G\phi_1 - Q_1\phi_2\right)x_3, \ a_{21} = Q_1^G - iR_1^G\phi_2 x_1, \\
a_{22} &= R_1^G - iR_1^G\phi_2 x_2, \ a_{23} = -iR_1^G\phi_2 x_3, \\
a_{31} &= Q_2^G + iR_2^G\phi_1 x_1, \ a_{32} = iR_2^G\phi_1 x_2, \\
a_{33} &= R_2^G + iR_2^G\phi_1 x_3, \\
b_{11} &= -\rho_{11}\omega^2 + i\omega(b_1 + b_2), \ b_{12} = -\rho_{12}\omega^2 - i\omega b_1, \\
b_{13} &= -\rho_{13}\omega^2 + i\omega b_2, \ b_{21} = -\rho_{12}\omega^2 - i\omega b_1, \\
b_{22} &= -\rho_{22}\omega^2 + i\omega b_1, \ b_{23} = 0, \\
b_{31} &= -\rho_{13}\omega^2 - i\omega b_2, \ b_{32} = 0, \\
b_{33} &= -\rho_{33}\omega^2 + i\omega b_2.
\end{aligned}$$

$$(B2)$$

and

$$x_1 = i(\phi_2 Q_1^G - \phi_1 Q_2^G)/Z^G, \ x_2 = i\phi_2 R_1^G/Z^G,$$

$$x_3 = -i\phi_1 R_2^G/Z^G,$$

$$\begin{aligned}
Z^G &= \frac{i\omega\eta\phi_1^2\phi_2\phi_{20}R_0^2}{3\kappa_{10}} - \frac{\rho_f\omega^2 R_0^2\phi_1^2\phi_{20}}{3\phi_{10}} \\
&\quad - \left(\phi_2^2 R_1^G + \phi_1^2 R_2^G\right), \\
A^G &= (1-\phi)K_s - \frac{2}{3}N^G \\
&\quad - \frac{\beta\phi_1(1-\phi_1-\phi_2-K_b/K_s)K_s^2/K_f}{\beta(1-\phi_1-\phi_2-K_b/K_s)+(\beta\phi_1+\phi_2)K_s/K_f} \\
&\quad - \frac{\phi_2(1-\phi_1-\phi_2-K_b/K_s)K_s^2/K_f}{1-\phi_1-\phi_2-K_b/K_s+(\beta\phi_1+\phi_2)K_s/K_f}, \\
Q_1^G &= \frac{\beta\phi_1(1-\phi_1-\phi_2-K_b/K_s)K_s}{\beta(1-\phi_1-\phi_2-K_b/K_s)+(\beta\phi_1+\phi_2)K_s/K_f}, \\
Q_2^G &= \frac{(1-\phi_1-\phi_2-K_b/K_s)\phi_2 K_s}{1-\phi_1-\phi_2-K_b/K_s+(\beta\phi_1+\phi_2)K_s/K_f}, \\
R_1^G &= \frac{(\beta\phi_1+\phi_2)\phi_1 K_s}{\beta(1-\phi_1-\phi_2-K_b/K_s)+(\beta\phi_1+\phi_2)K_s/K_f}, \\
R_2^G &= \frac{(\beta\phi_1+\phi_2)\phi_2 K_s}{1-\phi_1-\phi_2-K_b/K_s+(\beta\phi_1+\phi_2)K_s/K_f}, \\
N^G &= \mu_b,
\end{aligned}$$

$$(B3)$$

where β is the dilatation ratio between the fluid bulk strains in the host and inclusions. The complex wave velocity is used to compute the phase velocity (Carcione 2022),

$$V_P = \frac{\omega}{\text{Re}(k)}. \qquad (B4)$$

The P-wave quality factor is

$$Q = \frac{\text{Re}(k)}{2\text{Im}(k)}. \qquad (B5)$$

Conflict of interest statement. None declared.

References

Adam, L., Batzle, M., Lewallen, K.T. & Wijk, K., 2009. Seismic wave attenuation in carbonates. *Journal of Geophysical Research: Solid Earth*, **114**, B06208.

Ba, J., Carcione, J.M. & Nie, J.X., 2011. Biot-Rayleigh theory of wave propagation in double-porosity media. *Journal of Geophysical Research: Solid Earth*, **116**, B06202.

Ba, J., Zhang, L., Sun, W. & Hao, Z., 2014. Velocity field of wave-induced local fluid flow in double-porosity media. *Science China Physics, Mechanics & Astronomy*, **57**, 1020–1030.

Batzle, M. & Wang, Z., 1992. Seismic properties of pore fluids. *Geophysics*, **57**, 1396–1408.

Biot, M.A., 1956a. Theory of propagation of elastic waves in a fluid-saturated porous solid. I. Low-frequency range. *The Journal of the Acoustical Society of America*, **28**, 168–178.

Biot, M.A., 1956b. Theory of propagation of elastic waves in a fluid-saturated porous solid. II. Higher frequency range. *The Journal of the Acoustical Society of America*, **28**, 179–191.

Borgomano, J.V.M., Pimienta, L.X., Fortin, J. & Guéguen, Y., 2019. Seismic dispersion and attenuation in fluid-saturated carbonate rocks: effect of microstructure and pressure. *Journal of Geophysical Research: Solid Earth*, **124**, 12498–12522.

Cao, Z., Li, X.-Y., Liu, J., Qin, X., Sun, S., Li, Z. & Cao, Z., 2018. Carbonate fractured gas reservoir prediction based on P-wave azimuthal anisotropy and dispersion. *Journal of Geophysics and Engineering*, **15**, 2139–2149.

Carcione, J. & Gurevich, B., 2011. Differential form and numerical implementation of Biot's poroelasticity equations with squirt dissipation. *Geophysics*, **76**, N55–N64.

Carcione, J.M., 2022. *Wave Fields in Real Media: Wave Propagation in Anisotropic, Anelastic Porous and Electromagnetic media*, 4th edn. Elsevier Science.

Carcione, J.M., Helbig, K. & Helle, H.B., 2003. Effects of pressure and saturating fluid on wave velocity and attenuation in anisotropic rocks. *International Journal of Rock Mechanics and Mining Sciences*, **40**, 389–403.

Chapman, S., Tisato, N., Quintal, B. & Holliger, K., 2016. Seismic attenuation in partially saturated Berea sandstone submitted to a range of confining pressures. *Journal of Geophysical Research: Solid Earth*, **121**, 1664–1676.

David, E.C. & Zimmerman, R.W., 2012. Pore structure model for elastic wave velocities in fluid-saturated sandstones. *Journal of Geophysical Research: Solid Earth*, **117**, B07210.

Dvorkin, J., Mavko, G. & Nur, A., 1995. Squirt flow in fully saturated rocks. *Geophysics*, **60**, 97–107.

Grab, M., Quintal, B., Caspari, E., Deuber, C., Maurer, H. & Greenhalgh, S., 2017. The effect of boiling on seismic properties of water-saturated fractured rock. *Journal of Geophysical Research: Solid Earth*, **122**, 9228–9252.

Guo, J. & Gurevich, B., 2020. Frequency-dependent P-wave anisotropy due to wave-induced fluid flow and elastic scattering in a fluid-saturated porous medium with aligned fractures. *Journal of Geophysical Research: Solid Earth*, **125**, e2020JB020320.

Guo, J., Gurevich, B. & Chen, X., 2022a. Dynamic SV-wave signatures of fluid-saturated porous rocks containing intersecting fractures. *Journal of Geophysical Research: Solid Earth*, **127**, e2022JB024745.

Guo, J., Zhao, L., Chen, X., Yang, Z., Li, H. & Liu, C., 2022b. Theoretical modelling of seismic dispersion, attenuation and frequency-dependent anisotropy in a fluid saturated porous rock with intersecting fractures, *Geophysical Journal International*, **230**, 580–606.

Gurevich, B., Makarynska, D., Paula, O.B. & Pervukhina, M., 2010. A simple model for squirt-flow dispersion and attenuation in fluid-saturated granular rocks. *Geophysics*, **75**, N109–N120.

Jaya, M.S., Shapiro, S.A., Kristinsdóttir, L.H., Bruhn, D., Milsch, H. & Spangenberg, E., 2010. Temperature dependence of seismic properties in geothermal rocks at reservoir conditions. *Geothermics*, **39**, 115–123.

Jin, Z., Chapman, M. & Papageorgiou, G., 2018. Frequency-dependent anisotropy in a partially saturated fractured rock. *Geophysical Journal International*, **215**, 1985–1998.

Lee, M.W., 2006. A simple method of predicting S-wave velocity. *Geophysics*, **71**, F161–F164.

Mavko, G. & Nur, A., 1975. Melt squirt in the asthenosphere. *Journal of Geophysical Research*, **80**, 1444–1448.

Mori, T. & Tanaka, K., 1973. Average stress in matrix and average elastic energy of materials with misfitting inclusions. *Acta Metallurgica*, **21**, 571–574.

Mousavi, M., Prodanovic, M. & Jacobi, D., 2013. New classification of carbonate rocks for process-based pore-scale modeling. *SPE Journal*, **18**, 243–263.

Müller, T.M., Gurevich, B. & Lebedev, M., 2010. Seismic wave attenuation and dispersion resulting from wave-induced flow in porous rocks—a review. *Geophysics*, **75**, 147–164.

Pride, S.R., Berryman, J.G. & Harris, J.M., 2004. Seismic attenuation due to wave-induced flow. *Journal of Geophysical Research: Solid Earth*, **109**, B01201.

Rabbani, A., Schmitt, D.R., Nycz, J. & Gray, K., 2017. Pressure and temperature dependence of acoustic wave speeds in bitumen-saturated carbonates: implications for seismic monitoring of the Grosmont Formation. *Geophysics*, **82**, 1–72.

Ravalec, M., Guéguen, Y. & Chelidze, T., 1996. Elastic wave velocities in partially saturated rocks: saturation hysteresis. *Journal of Geophysical Research: Solid Earth*, **101**, 837–844.

Shapiro, S.A., 2003. Elastic piezosensitivity of porous and fractured rocks. *Geophysics*, **68**, 482–486.

Tang, X., 2011. A unified theory for elastic wave propagation through porous media containing cracks—an extension of Biot's poroelastic wave theory. *Science China Earth Sciences*, **54**, 1441–1452.

Timur, A., 1968. Velocity of compressional waves in porous media at permafrost temperatures. *Geophysics*, **33**, 584–595.

Toksöz, M.N., Johnston, D.H. & Timur, A., 1979. Attenuation of seismic waves in dry and saturated rocks: I. Laboratory measurements. *Geophysics*, **44**, 681–690.

Tran, D.T., Rai, C.S. & Sondergeld, C.H., 2008. Changes in crack aspect-ratio concentration from heat treatment: a comparison between velocity inversion and experimental data. *Geophysics*, **73**, E123–E132.

Wu, C., Ba, J., Carcione, J.M., Fu, L.-Y., Chesnokov, E.M. & Zhang, L., 2020. A squirt-flow theory to model wave anelasticity in rocks containing compliant microfractures. *Physics of the Earth and Planetary Interiors*, **301**, 106450.

Xi, D., Liu, X. & Zhang, C., 2007. The frequency (or time)-temperature equivalence of relaxation in saturated rocks. *Pure and Applied Geophysics*, **164**, 2157–2173.

Xu, S. & Payne, M.A., 2009. Modeling elastic properties in carbonate rocks. *The Leading Edge*, **28**, 66–74.

Zhang, L., Ba, J. & Carcione, J.M., 2021. Wave propagation in infinituple-porosity media. *Journal of Geophysical Research: Solid Earth*, **126**, e2020JB021266.

Zhang, L., Ba, J., Carcione, J.M. & Wu, C., 2022. Seismic wave propagation in partially saturated rocks with a fractal distribution of fluid-patch size. *Journal of Geophysical Research: Solid Earth*, **127**, e2021JB023809.

Zhang, L., Ba, J., Fu, L., Carcione, J.M. & Cao, C., 2019. Estimation of pore microstructure by using the static and dynamic moduli. *International Journal of Rock Mechanics and Mining Sciences*, **113**, 24–30.